HHS Public Access

Quantitative imaging of disease signatures through radioactive decay signal conversion

Daniel LJ Thorek[1], **Anuja Ogirala**[1], **Bradley J Beattie**[2], and **Jan Grimm**[1,3]

[1]Department of Radiology, Memorial Sloan-Kettering Cancer Center, New York, New York

[2]Department of Medical Physics, Memorial Sloan-Kettering Cancer Center, New York, New York

[3]Program in Molecular Pharmacology and Chemistry, Memorial Sloan-Kettering Cancer Center, New York, New York

Abstract

In the era of personalized medicine there is an urgent need for *in vivo* techniques able to sensitively detect and quantify molecular activities. Sensitive imaging of gamma rays is widely used, but radioactive decay is a physical constant and signal is independent of biological interactions. Here we introduce a framework of novel targeted and activatable probes excited by a nuclear decay-derived signal to identify and measure molecular signatures of disease. This was accomplished utilizing Cerenkov luminescence (CL), the light produced by β-emitting radionuclides such as clinical positron emission tomography (PET) tracers. Disease markers were detected using nanoparticles to produce secondary Cerenkov-induced fluorescence. This approach reduces background signal compared to conventional fluorescence imaging. In addition to information from a PET scan, we demonstrate novel medical utility by quantitatively determining prognostically relevant enzymatic activity. This technique can be applied to monitor other markers and facilitates a shift towards activatable nuclear medicine agents.

Keywords

Activatable probes; Molecular imaging; Nanoparticles; Cerenkov luminescence

INTRODUCTION

Radioisotopes play a fundamental role in life sciences and clinical medicine, enabling unparalleled sensitivity in applications to study and identify disease. However, the physical phenomenon of radioactive decay cannot be switched between 'on' and 'off' states. Radiolabeled molecules are always detectable regardless of their biological interactions (Fig.

1a). This has so far excluded nuclear approaches from use as "activatable probes"; these are agents whose signal is released upon interaction with their biologic target. Clinical radiotracers such as [^{18}F]-fluorodeoxyglucose ([^{18}F]-FDG) and radiotracer genetic reporters[1,2] indirectly report metabolic activity through accumulation and are plagued by high background signals.

Activatable optical and magnetic resonance (MR) imaging have visualized enzyme activity implicated in inflammation, cancer aggressiveness and progression[3–5]. Ideally, molecular imaging accurately reports activity of an enzyme or other biological event at a disease site. Fluorescence or bioluminescent strategies are powerful, but are inherently non-quantitative with instrument-dependent results. Likewise, MR only reveals relative relaxivity changes dependent on an unknown probe concentration[6]. Similar caveats hold for newer approaches involving PET[7].

Cerenkov luminescence (CL) is light generated when charged particles (e.g. β$^-$ and β$^+$ particles emitted upon radioactive decay) exceed the speed of light in a dielectric medium (Fig. 1b). First observed over a century ago[8], visualization of CL was only recently achieved *in vivo*[9]. Advantages of CL include higher throughput, cost savings and greater surface resolution compared to nuclear imaging (Supplementary Fig. 1). Produced by many clinically approved tracers, it offers a facile route for translation of optical molecular imaging[10,11].

Here we describe a new imaging strategy that utilizes nanoparticles (NP) to achieve activatable imaging through biologically-specific fluorescent conversion of CL; secondary Cerenkov-induced fluorescence imaging (SCIFI; Fig. 1c). This is used in the form of an activatable imaging agent for the detection of clinically relevant enzymatic activity. We overcome issues of target specificity, background noise, tracer clearance and quantitation through unique combinations of PET and nanoparticle-CL imaging. We hypothesize that nuclide-based activatable imaging will enable specific imaging of disease signatures for the benefit of biomedical research and clinical diagnostic accuracy.

RESULTS

Fluorescence and Cerenkov-Induced Fluorescence

CL conversion to a longer wavelength by a fluorophore was demonstrated in an *in vitro* phantom model. We mixed a CL source (gallium-68) with fluorescein (FAM) in a quartz vial and submerged it in a tissue scattering and absorbing medium to compare conventional fluorescence with SCIFI (Fig. 2a,b). Defining regions of interest over the source and background, it was found that the incident excitation light (required for conventional fluorescence) adversely affected the signal-to-background distinction (Fig. 2c). In contrast, internal excitation by the radionuclide for SCIFI significantly decreased the non-specific signal, resulting in greater signal-to-background values (Fig. 2d). These results persisted at increasing depth, where we had assumed that the lower photon flux of the Cerenkov source would diminish any advantage.

Complicating conventional fluorescence imaging is skin autofluorescence and reflection from excitation light. Mimicking a tumor xenograft, [^{18}F]-FDG was used in tandem with fluorescein and subcutaneously implanted. The exciting light for conventional fluorescence, which must first scatter and penetrate into the tissue to excite the fluorophore, increased background signal (Fig. 2e–g). Following quantitation, the signal-to-background values for SCIFI were 5.7–times greater than that of the conventional imaging (Fig. 2h). These results indicate that sensitive and low background acquisitions are advantages of SCIFI despite the low light intensity.

Multispectral co-dependent imaging of tumor markers

PET enables tomographic, whole-body and quantitative imaging, but can only evaluate a single tracer per study. We sought to achieve multiparameter readout of the molecular pathophysiology of disease by converting CL from PET tracers with spectrally distinct fluorophores in addition to acquiring PET data.

The continuous CL spectrum is primarily blue; less than optimal for *in vivo* imaging. However, this spectrum can excite many widely used fluorophores. Therefore, we pursued CL-excited fluorescent NP (quantum dots; QD) emitting in the deeper tissue-penetrating near-infrared (Fig. 3a,b)[12,13]. We used [^{18}F]-FDG to evaluate emissions from an array of fluorophores (Fig. 3c; an unmasked, equalized scale image is presented as Supplementary Fig. 2). The agents tested evaluate SCIFI across a broad range of spectral wavelengths (Supplementary Tables 1,2).

Analysis indicated that the excitation profile of the fluorescein-based FITC and QDs are optimal for SCIFI, particularly QD605 (Fig. 3c). Cyanine dyes are less well suited due to excitation outside of the main CL emission[14]. The three QDs evaluated possess distinct fluorescent emission characteristics for SCIFI *in vitro* (Supplementary Fig. 3a) and *in vivo,* contained in matrigel pseudo-tumors (Supplementary Fig. 3b).

SCIFI enables multispectral, deep tissue and potentially targeted imaging from the radiotracer source. We hypothesized that we could independently target a clinical radiotracer and QD to simultaneously demonstrate multiparameter imaging of tumor signatures with high tumor-to-background. [^{89}Zr]-DFO-trastuzumab (undergoing clinical trial for metastatic breast cancer detection[15]) was administered to mice bearing Her2/neu-positive tumor xenografts (BT-474). Uptake of [^{89}Zr]-DFO-trastuzumab (6 h p.i.) was followed by PET and CL. As expected, the targeted radiotracer revealed the presence of Her2/neu expression of the xenografts (Fig. 3d).

We next injected QD605 targeting the $\alpha_v\beta_3$ integrin (cyclic-RGD QD605) or control QD605 (cyclic-RAD peptide). SCIFI signal was generated by excitation of the co-localized [^{89}Zr]-DFO-trastuzumab and cyclic-RGD QD, but was absent in the nonspecific control (Fig. 3d). Selective co-dependent signal can be observed non-invasively over the experiment's duration; showing injection, binding and clearance (Fig. 3e).

No autofluorescence or reflection from external excitation results in minimal background, and greater than four times the signal from the targeted probe is seen at 2 h (Fig. 3f). SCIFI

provides this information in addition to the quantitative radiotracer uptake data assessing Her2 expression (across both groups at 18 h p.i.; $11.56\pm1.08\%$ ID g^{-1}). Following demonstration of PET and SCIFI for determination of multiple disease relevant ligands concomitantly, we sought to distinguish *in vivo* activation of a SCIFI probe.

In vivo imaging of MMP-2 enzymatic activity

Gold nanoparticles (AuNP) were conjugated to FAM-labeled peptides as a biocompatible activatable platform to measure disease-relevant enzymes (Fig. 4a). The peptide sequence, *Ile-Pro-Val-Ser-Leu-Arg-Ser-Gly* (*IPVSLRSG*), is cleaved at the *Ser-Leu* bond[16] by the gelatinase MMP-2 (implicated in cancer aggressiveness[17–19]). Coupling of the peptide to the AuNP surface, AuNP-IPVSLRSG-FAM, quenches FAM fluorescence[20]. MMP-2 cleavage releases FAM and its emission becomes detectable (Fig. 4b). We hypothesized that the [18F]-FDG CL-excited fluorescence (Fig. 4c) could be spectrally separated from CL to quantitate the activation of the probe and therefore read-out both glycolytic ([18F]-FDG) and enzymatic activity (MMP-2).

Mice bearing MMP-2-overexpressing (SCC7) and low expressing (BT20) xenografts[21] were co-injected with [18F]-FDG and AuNP-IPVSLRSG-FAM. [18F]-FDG had slightly preferential but non-significant ($p > 0.2$) uptake in the faster-growing SCC7 tumors by PET (Fig. 4d). Optical imaging (open, no filter) recapitulated the negligible difference ($p > 0.1$) between tumor types (Fig. 4e). However, SCIFI imaging using a bandpass filter for FAM revealed statistically significant activated signal (*$p < 0.001$*), solely in SCC7 tumors (Fig. 4f). We performed X-ray computed tomography and dark-field microscopy to remove the possibility that the difference was due to differential probe distribution (Supplementary Information and Supplementary Fig. 4). Successful SCIFI by MMP-2 cleavage provides molecularly specific information atop the indiscriminate [18F]-FDG uptake via PET.

Next, we quantitated activation of the NP probe, an obvious advance over merely detecting activation. PET accurately reveals the actual radiotracer concentration. This can be used with the integrated Frank-Tamm equation to calculate the amount of CL produced in a defined spectral window in tissue[22]. We first separated the filtered signal (510–575 nm) from its two components: the activated SCIFI probe (FAM) and the remaining CL contribution (Fig. 4g; additional information in Supplementary Fig. 5 and Methods). We determined the number of activated probes using a calibration curve of CL-excited FAM. In the enzyme-expressing tumor, this yields an average of 6.23 pmol of activated probe, whereas activation in the control tumor was 1.56 pmol ($p < 0.001$) (Fig. 4h). We also analyzed the expression and gelatinolytic activity of MMP-2 from cell culture supernatant and excised tumors. Expression of activated-MMP-2 was greater on a per total-protein basis in the culture supernatant (SCC7: 31.8 ng, BT20: 5.83 ng) than in the lysed tumors (SCC7: 1.16 ng, BT20: 0.187 ng; Fig. 4i). Zymography of representative tumor lysates revealed an enzyme activity of 1.49 and 2.21 ng (Fig. 4j). Relative differences between quantative western blot data as well as the enzyme activity correlate well with *in vivo* SCIFI assessment of protease activation.

DISCUSSION

These results establish that targeted and activatable fluorescent probes can transfer and spectrally shift the optical radionuclide decay signal of Cerenkov radiation from clinical radionuclides. SCIFI distinguishes with high-specificity, low background and high-resolution (superficially) the presence of multiple molecular signatures of disease. This inherently dual–modality approach first uses systemically administered agents to achieve whole-body quantitative radionuclide distribution by PET. Multiple molecular features of the tumor environment are then captured using fluorescent NP sensors excited by the radiotracer. This approach has the potential to create a new application space for nuclear molecular imaging.

Quantitative PET signal indicates increased glycolytic activity (e.g. in malignancies), and this remains unaltered by the optical probes. SCIFI reveals biomolecularly specific information regarding tumor biology such as marker expression (eg. $\alpha_v\beta_3$). This work motivates a first approach for using radiotracers as platforms for activatable agents as we show quantitative readout of probe activation by an enzyme (eg. MMP-2). This yields complementary information otherwise unobtainable with PET alone, which cannot distinguish signal from multiple tracers or between activated and non-activated agent. Multispectral SCIFI was illustrated through the simultaneous excitation of multiple fluorophores *in vitro* (Fig. 2b) and of three reporters with a single administration of [^{18}F]-FDG *in vivo* (Supplemental Fig. 3).

Using this approach, SCIFI visualized both Her2/neu and $\alpha_v\beta_3$ to simultaneously readout multiple disease-relevant markers. This required no external excitation of agent; antibody and QD were detected as a result of co-dependent CL and secondary-Cerenkov emission, respectively. SCIFI is dependent on the distribution of the targeted radioactive and optical probes, requiring biospecific homing (via trastuzumab and RGD peptide, respectively). Unlike other activatable approaches, such as bioluminescence resonance energy transfer[23,24], the systems described herein do not require administration of immunogenic proteins (e.g. luciferase and green fluorescent protein) or foreign enzyme substrate (e.g. luciferin or coelenterazine). SCIFI avoids reflection and autofluorescence artifacts from external excitation and achieves minimal background signal by utilizing internal illumination through CL.

Successful application of SCIFI did not require toxic QD, and was accomplished with inert AuNP and approved dye. Activated AuNP fluorescent conversion of CL from tumor non-specific [^{18}F]-FDG resolved specific enzymatic expression of distinct tumors. Significantly, tumors or sites of inflammation are often identified solely through increased glycolysis and accumulation of [^{18}F]-FDG, oblivious to other important molecular markers[25]. Non-invasive distinction of tumor-to-tumor molecular heterogeneity, quantitatively, is a critical step towards personalization of diagnosis and patient management.

CL intensity is dependent on the energy of the emitted charged particle and properties of the surrounding medium[26]. The low amount of light (relative to fluorescence) can be detected by high-sensitivity cameras[9], but translation to the clinic presents technical challenges

including strict restriction of ambient light and tissue depth-dependent signal attenuation. Greater CL producing radionuclides (such as ^{68}Ga and [89]Zr) can be used to overcome some signal level concerns. Application specific instrumentation (e.g. adapted endoscopy) can also be expected to reduce the difficulty of translation[27,28]. Whole-body optical imaging is likely not feasible, however hybrid SCIFI-PET overcomes some depth and imaging issues over conventional fluorescence.

Offering an impact beyond small-animal imaging, clinically approved tracer and fluorophore combinations lessen regulatory issues associated with clinically-untested compounds. This is an issue that has hindered translation of conventional fluorescence agents. With the requirement of sensitive camera equipment, SCIFI could be translated to the clinic in diagnostic and intraoperative settings with minor deviation from current protocols.

The systems used here enable target specific and activatable investigation of multiple biological signatures *in vivo*, through the fluorescent conversion of a radioactive decay signal. Clinical radiotracers in concert with diagnostic and therapeutic NP sensors targeted to the ever-expanding library of disease markers lend this novel methodology to an array of basic and potentially clinical applications. The synergistic advantages of PET in addition to Cerenkov-optical imaging provide strong impetus for further investigation.

ONLINE METHODS

Chemicals

All materials were purchased from Thermo Fisher Scientific (Waltham, MA), unless otherwise noted. Quantum dots (QD565, QD605 and QD800; amino-PEG-ITK) were purchased from Invitrogen. Cy5.5-NHS and Cy7-NHS were purchased from GE Healthcare. All peptides were obtained from Anaspec Incorporated. QD conjugates and AuNP and were synthesized as described below.

Radionuclides and Tracers

[^{18}F]-fluorodeoxyglucose ([^{18}F]-FDG) was supplied by IBA Molecular with a specific activity of >41 MBq/μmol (>11 mCi/μmol) and a radiochemical purity of >98%. The tracer was obtained through the Radiopharmacy of the Department of Nuclear Medicine at Memorial Sloan-Kettering Cancer Center (MSKCC). 0.1 N HCl ^{68}Ga elute was obtained from a [68]Ge/^{68}Ga generator.

[[89]Zr] was obtained from the Radiochemistry Core Facility. It is produced in high radiochemical and radionuclidic purity via the [89]Y(p,n)[89]Zr transmutation reaction on an Ebco TR19/9 variable beam-energy cyclotron (Ebco Industries Incorporated)[29]. [[89]Zr] was purified and used to label the monoclonal antibody trastuzumab (Genentech) as previously described[30].

Nanoparticle Probes

Quantum Dot Probes—QD605 was used as the basis to construct targeted and activatable fluorescent nanoparticle probes. This is a near infrared agent that adequately matches the 600 +/−10 nm bandpass filter on the IVIS 200 system. For targeted *in vivo*

imaging, $\alpha_v\beta_3$ integrin targeting particles were linked to Cyclo-(RGDyK), while control particles were coupled to Cyclo-(RADfK)[31]. QD605 was coupled to peptides following activation with disuccinimidyl suberate (DSS) in pH 8.5 Na_2CO_3 buffer. After 1 h incubation, the particles were purified with a YM-50 filter (Millipore) and functionalized with the peptide.

Gold Nanoparticle Probes—Citrated-capped gold nanoparticles (AuNP) were synthesized by dissolving 50 mg of hydrogen tetrachloroaurate trihydrate in 150 mL of dH_2O. Sodium citrate (15 mL, 40 mM) was added to a boiling solution of the chlorauric acid. Unreacted components were removed by centrifugal purification prior to conjugation. The peptide, Cys-$(PEG)_2$-IPVSLRSG-$(PEG)_2$-Lys(5-FAM)-Gly-Lys(DOTA), was added in 100x molar excess to the particles, mixed overnight at 15 °C, and then purified through repeated washes in saline on a YM-50 filter. Peptide labeled particles were fully soluble in physiological buffers at pH 7.4.

Spectrophotometry

All probes and radionuclides were characterized for absorbance and luminescent properties using a SpectraMax M5 (Molecular Devices). All samples were read using a quartz cuvette (volumes between 250 and 1000 μL). All QD fluorescent profiles were obtained with excitation at the 488 nm laser line. Cerenkov excited fluorescent profiles of the QD were obtained by comixing the particles with ^{68}Ga (270 μCi; 10 MBq) and capturing the luminescence spectra.

Animal Experiments

All animal experiments were conducted in compliance with Institutional Animal Care and Use Committee guidelines and the Guide for the Care and Use of Laboratory Animals[32]. All animal procedures were performed under anesthesia by inhalation of a 1–4% isoflurane-air mixture (Baxter Healthcare). Animals were obtained from Harlan Laboratories. Athymic Nu/Nu mice between the ages of 10–16 weeks were used for all experiments. Female mice were used for the [^{89}Zr]-DFO-trastuzumab studies (approximately 260 μCi per mouse; 9.62 MBq) and male mice were used in all other experiments.

Cerenkov Luminescence (CL) Imaging

CL images were obtained using the IVIS 200 run under Living Image 4.2 (Caliper Life Sciences). This system utilizes a cryo-cooled EMCCD for high sensitivity detection of low light sources. Filters provided with the device determined to some degree the fluorophores and QD tested. All images were quantitated in the Living Image software (version 2.6).

For the determination of the signal to background ratio of Cerenkov in a tissue mimic phantom, 150 μCi or 5.55 MBq of [^{68}Ga] activity was placed in a glass vial filled with glycerin. For evaluation of dye and QD particles activation properties, 14.8 MBq (400 μCi) of [^{18}F]-FDG (200 μL in an Eppendorf tube) was used. The source was surrounded by 100 μL volume solutions of water, FITC, Cy dyes (at 1 mM) and QD (4 μM) samples. The subcutaneously implanted [^{18}F]-FDG (55 μCi; 2.04 MBq) was placed in a capillary tube, with or without comixture with fluorescein. For *in vivo* excitation of multiple quantum dots

simultaneously, a dose of [^{18}F]-FDG (660 μCi, 24.42 MBq) was administered to the animal immediately before imaging.

Phantom Imaging for SCIFI and Fluorescence Comparison

***In vitro* phantom**—A vial (0.7 mm inner diameter×2.5 cm in length) was filled with a mixture of glycerine (refractive index of 1.47), radionuclide (freshly eluted gallium-68 balanced to pH 7.4 with sodium carbonate) and fluorophore (FAM). The final concentration of fluorophore was 0.5 mM and the starting activity of the ^{68}Ga was 150 μCi (5.55 MBq). The vial was placed in a black container, in a tissue scattering and absorbing phantom composed of Intralipid (Fresenius Kabi) and India ink (Fisher Scientific)[33]. Imaging was performed on the IVIS 200 (Calipers), using the GFP excitation (for fluorescence) and emission filters, and all results were decay corrected to the initial acquisition. Increasing volume of the scattering and absorbing media were added, and the depth calculated from the dimensions of the container. Images were acquired for 30 seconds. Regions of interest were drawn around the vial when it was exposed (prior to be submerged) along with multiple regions of interest at the corners of the container. Background subtracted signal-to-background measurements were made off of these regions, using average radiance (ph s^{-1} cm^{-2} sr^{-1}).

***In vivo* phantom**—A capillary tube was filled with saline, FAM (0.5 mM) and [^{18}F]-FDG (115 μCi, 4.26 MBq). This was then subcutaneously implanted into a euthenized mouse. Images were acquired for 60 seconds. The experiment was performed in triplicate.

Fluorescence Imaging and SCIFI

For *in vivo* multispectral conventional fluorescence imaging, the Maestro was used. Multispectral SCIFI was done with acquisitions on the IVIS 200 in the 560 and 600 nm bandpass and ICG filters. Luminescent images without Cosmic Ray correction were imported into ImageJ and outliers were then removed. The filter specific images were false colored and then overlaid on a white light image of the animal. Individual channel acquisitions can be found in Supplementary Fig. 5b. Activatable SCIFI imaging to detect MMP-2 enzyme activity was performed with the GFP filter using the IVIS 200. The luminescent images were exported and processed in ImageJ, as above.

PET

Mice were imaged in a prone position using either an R4 or Focus 120 microPET™ dedicated small-animal PET scanner (Concorde Microsystems Inc.), with an energy window of 350–700 keV and coincidence timing window of 6 ns. For [^{18}F]-FDG studies, images were acquired at 60 minutes post-administration over a period of 15 minutes. Times of acquisition for [^{89}Zr] studies were also 15 minutes in length, at the post-injection times noted.

The list-mode data were sorted into 2D histograms by Fourier re-binning and images reconstructed by filtered back-projection using a ramp filter with a cut-off frequency equal to the Nyquist frequency in either a 128×128×64 matrix (R4) or a 128×128×94 matrix

(Focus 120). Normalized image data (ie. corrected for non-uniformity of scanner response) was corrected for dead time count losses and physical decay to the time of injection.

Count rates in the reconstructed images were converted to activity concentration and subsequently percent of injected dose per gram of tissue (percentage injected dose g^{-1}) using a system calibration factor (μCi mL^{-1} cps^{-1} voxel^{-1}) derived from imaging a mouse-size phantom filled with a uniform aqueous solution of [^{18}F]-FDG. The reconstructed images were visually examined and analyzed using ASIProVM (Concorde Microsystems Inc.) with window and level settings adjusted for maximal tumor visibility. ROI were manually drawn to circumscribe tumors. The mean percentage injected dose g^{-1} within the structure was computed from the volume of interest. For [^{18}F]-FDG acquisitions, animals were deprived of food for between 4 and 6 h prior to imaging.

Quantification Model

Quantitation of the dye molecules activated was achieved through observed measurements and modeling. We determine the number of Cerenkov photons generated from the radioactivity accumulated in a tumor by integrating the Frank-Tamm equation (1) for the β-particle energy distribution of ^{18}F over the Cerenkov threshold between the relevant wavelengths[34]. This is the emission regions (510–570 nm) of the FAM or GFP filter.

$$\frac{dN}{dx} = 2\alpha\pi \left(\frac{1}{\lambda_2} - \frac{1}{\lambda_1} \right) \left(1 - \frac{1}{(\beta n)^2} \right) \quad (1)$$

Here β is the velocity of the particle relative to the speed of light, n is the refractive index, dN/dx is the number of photons produced per cm path length and α is fine-structure constant. From the PET quantitation of activity, we can determine the number of photons produced in the 510–570 nm range. At a tissue refractive index estimated from the literature of 1.4, and the activity as measured from PET, this gives a value of 0.4206 photons/Bq. This was then adjusted for attenuation using an experimentally determined factor, derived from observed photon flux in the tumors with [^{18}F]-FDG 72 h prior to the activation experiments. Subtracting this value from the observed tumor photon flux yields the contribution from the active fluorescent probe alone. Utilizing an experimentally determined standard curve of the active probe (AuNP and FAM) in saline (n=1.33) and [^{18}F]-FDG, we can determine the number of activated FAM molecules from the observed SCIFI channel.

X-Ray Computed Tomography (CT) Imaging

Imaging for detection of gold nanoparticle uptake was performed using a microCAT II (ImTek Inc.) scanner operating at 60 kVp and 0.8 mA with 2 mm aluminum filtration. Animals injected with the AuNP and without were scanned. All animals bore dual-shoulder xenografts of BT20 (MMP2–) and SCC7 (MMP2+) tumors. Images were acquired with a 93 μm isotropic resolution. A global ROI was drawn around the animal and zero-filled to exclude edge and bed signal. Data for 5 sequential slices through each tumor were evaluated for intensity in each tumor, paraspinal muscle and air (analyzed in ImageJ). A reconstruction using the ImageJ 3D volume viewer plugin was used to create the three-dimensional slab view.

Quantitative Western Blotting

Cell supernatants were obtained using serum free media from BT-20 and SCC7 cultures and concentrated using Amicon Ultra centrifugal filters (5, 000 MWCO). BT-20 and SCC7 tumors were lyzed using 50 mM Tris pH 7.5, 150 mM NaCl and manually homogenized. Concentrated cell supernatants, tumor lysates and MMP-2 recombinant protein (Enzo Life Sciences) were activated by 1 mM 4-aminophenylmercuric acetate for 16 h at 37° C[35]. Cell supernatant (50 μg) and tumor lysate (30 μg) concentration were determined by the BCA assay. Samples were separated on NuPAGE 4–12 % Bis-Tris gels and electrophoretically transferred to nitrocellulose alongside MMP-2 standards (4 ng^{-1}; #BML-SE503). For MMP-2, membranes were incubated with anti-MMP-2 (Abcam; #ab37150; 1:1000) followed by donkey anti-rabbit 680RD (Licor; #926–68073; 1:1000), while the loading control was stained with anti-beta-actin (Sigma; #A1978; 1:1000) followed by goat anti-mouse (Licor; #926–68070; 1:5000). Blocking was performed in Odyssey Blocking Buffer (Licor) and the membranes were then imaged and analyzed using the Odyssey Infrared Imaging System (Licor) and ImageJ.

Quantitative Zymography

Unconcentrated cell supernatants and tumor lysates were prepared as above and gel loadings were determined by BCA assay (5 μg and 15 μg for cell supernatants and tumor lysates respectively). Samples were then loaded onto 10% Zymogram (gelatin) Gels (Life Technologies) alongside MMP-2 standards (250 pg - 20 ng) and run at 110V at 4 °C for 3.5 h. Gels were incubated in renaturing buffer (2.5% Triton-X 100) for 30 min at room temperature and transferred to developing buffer (50 mM Tris pH 8, 5 mM CaCl$_2$, 200 mM NaCl, 0.02% Brij) at 37 °C for 16–20 h. Following this treatment, gels were stained in Coomassie for 2–3 h and then destained to resolve digested (white) bands. Zymographies were finally imaged and analyzed using the ImageStation 4000R Pro (Carestream) and ImageJ.

Dark Field Microscopy

Approximately 1 h after probe was injected and imaged, animals were sacrificed and tumors removed. The tissue was embedded in OCT and sectioned at 10 μm thickness. Tissue was either dehydrated and image using dark-field, or stained for heamotoxylin and eosin using conventional microscopy. For dark field-imaging, a DarkLight slide illuminator mounted onto the slide stage of a Nikon Eclipse was used. H&E imaging was performed on a NikonTi inverted microscope. A 10x objective was used and images were captured on a SPOT RT camera (Diagnostic Instruments, Inc). For analysis, the number of particles or particle clusters were counted in ImageJ averaged over 10 fields.

Phantom Imaging for PET and Cerenkov Resolution

A miniature Jaczeck phantom was filled with a mixture of activity (gallium-68; 255 μCi, 9.43 MBq) dissolved in 15:1 saline:ethanol. The diameter of the rods in the phantom are 1.0 to 1.5 mm in 0.1 mm increments, arranged in 6 sextants. The core is a 2 mm central pillar. Imaging of the phantom on the small-animal imaging PET (R4, Concorde Microsystems) was completed following acquisition of 22×10^6 events. The image set was reconstructed

without attenuation correction using the maximum a priori algorithm which incorporates knowledge about the scanner's system matrix. A profile through the phantom was drawn and the intensity values plotted (ASI Pro VM Software, Concode Microsystems).

White light photography and Cerenkov luminescence images were acquired using the XR-Mega10Z camera with Schneider f0.95 lens in a custom designed light tight box (Stanford Photonics). The XR-Mega10Z is a dual microchannel plate gain stage (GaAsP) intensified camera (Sony XX285 sensor). Triplicate acquisitions were acquired and analyzed using the Piper software suite (Stanford Photonics). The decision to utilize the XR-Mega10Z was motivated in part to use alternative hardware to the IVIS systems (which have, to date, been the only hardware used to image Cerenkov radiation in small animals). An optically transparent vessel of known dimensions was placed above the resolution phantom. Increasing volume of scattering and absorbing tissue mimic liquid was added to simulate increasing tissue depth. Decay corrected intensity profiles, oriented identical to the PET acquisition, were drawn for each acquisition.

Background Radiation Detection

In order to evaluate the role of high-energy photons emitted from Cerenkov sources, we analyzed signals from a well filled with activity in an opaque black 24-well microplate (Grenier), with and without coverage by an opaque covering, and with and without so-called Cosmic ray correction (CRC). Cosmic ray correction is performed to remove signal from extraterrestrial high-energy particles that register on sensitive optical imaging equipment. These interactions with a CCD (IVIS 200) or intensifier screen (XR-Mega10Z) are detected as hot pixels with large signals. As described by the instruction manual for the IVIS 200, the Living Image software searches for isolated, high amplitude hot pixels and replaces them with collective average of surrounding pixels.

Plates were filled with [^{18}F]-FDG at 99.28, 12.59 and 1.10 MBq and diluted to 650 μL of total volume using deionized water. The plates were imaged at the maximum field of view of the system for 1 minute. Subsequently, the samples were covered with 10 sheets of black paper (Stratmore Artagain 400 Series Coal Black Drawing Paper). Signal from the well, background with and without covering were analyzed following decay correction of the signals.

As the IVIS imaging system performs automated background and CRC, we further investigated manual hot pixel removal. To this end, luminescent images of PC3 tumor bearing mice imaged 70 min after 7.12±0.07 MBq retro-orbital administration of [^{18}F]-FDG were imported into ImageJ. Two hot pixel filtering functions were used. In the first, a selective median filter that replaced the value of a pixel if it deviated from the median (in a 2 pixel radius) by greater than a given threshold (75 arbitrary units) by that median value. The second technique was to apply a median filter that replaced each pixel with the median value of the pixels surrounding it in a 3x3 neighborhood. No background luminescent or read bias correction was applied to these images, and thus the units remain uncorrected arbitrary units.

Additionally, in the case of the high frame rate XR-Mega10Z (120 fps), real-time removal of Cosmic ray event containing frames can be performed. This technique was effectively used

to remove any high-energy photons emitted from a Cerenkov source that struck the detector for the purposes of testing the resolution phantom.

Statistical Analysis

Statistical comparisons were made using the Mann-Whitney-Wilcoxon rank sum test. All experiments were performed in triplicate unless otherwise indicated.

Supplementary Material

Refer to Web version on PubMed Central for supplementary material.

ACKNOWLEDGEMENTS

REFERENCES

1. Miyagawa T, et al. Imaging of HSV-tk Reporter gene expression: comparison between [18F]FEAU, [18F]FFEAU, and other imaging probes. J Nucl Med. 2008; 49:637–648. [PubMed: 18344433]

2. Tjuvajev JG, et al. Comparison of radiolabeled nucleoside probes (FIAU, FHBG, and FHPG) for PET imaging of HSV1-tk gene expression. J Nucl Med. 2002; 43:1072–1083. [PubMed: 12163634]

3. Thorek DL, Grimm J. Enzymatically activatable diagnostic probes. Curr Pharm Biotechnol. 2012; 13:523–536. [PubMed: 22214507]

4. Grimm J, et al. Use of gene expression profiling to direct in vivo molecular imaging of lung cancer. Proceedings of the National Academy of Sciences of the United States of America. 2005; 102:14404–14409. [PubMed: 16183744]

5. Weissleder R, Tung CH, Mahmood U, Bogdanov A Jr. In vivo imaging of tumors with protease-activated near-infrared fluorescent probes. Nat Biotechnol. 1999; 17:375–378. [PubMed: 10207887]

6. Rudin M, Weissleder R. Molecular imaging in drug discovery and development. Nat Rev Drug Discov. 2003; 2:123–131. [PubMed: 12563303]

7. Chuang CH, et al. In vivo positron emission tomography imaging of protease activity by generation of a hydrophobic product from a noninhibitory protease substrate. Clin Cancer Res. 2012; 18:238–247. [PubMed: 22019516]

8. L'Annunziata, MF., et al. Radioactivity : introduction and history. Oxford: Elsevier; 2007.

9. Robertson R, et al. Optical imaging of Cerenkov light generation from positron-emitting radiotracers. Phys Med Biol. 2009; 54:N355–N365. [PubMed: 19636082]

10. Ruggiero A, Holland JP, Lewis JS, Grimm J. Cerenkov luminescence imaging of medical isotopes. J Nucl Med. 2010; 51:1123–1130. [PubMed: 20554722]

11. Liu H, et al. Molecular Optical Imaging with Radioactive Probes. PLoS One. 2010; 5:e9470. [PubMed: 20208993]

12. Dothager RS, Goiffon RJ, Jackson E, Harpstrite S, Piwnica-Worms D. Cerenkov Radiation Energy Transfer (CRET) Imaging: A Novel Method for Optical Imaging of PET Isotopes in Biological Systems. PLoS One. 2010; 5:e13300. [PubMed: 20949021]

13. Liu H, et al. Radiation-Luminescence-Excited Quantum Dots for in vivo Multiplexed Optical Imaging. Small. 2010; 6:1087–1091. [PubMed: 20473988]

14. Jelley JV. Cerenkov radiation and its applications. British Journal of Applied Physics. 1955; 6:227.

15. Dijkers EC, et al. Biodistribution of 89Zr-trastuzumab and PET Imaging of HER2-Positive Lesions in Patients With Metastatic Breast Cancer. Clin Pharmacol Ther. 2010; 87:586–592. [PubMed: 20357763]

16. Turk BE, Huang LL, Piro ET, Cantley LC. Determination of protease cleavage site motifs using mixture-based oriented peptide libraries. Nat Biotech. 2001; 19:661–667.

17. Väisänen A, Kallioinen M, Taskinen PJ, Turpeenniemi-Hujanen T. Prognostic value of MMP-2 immunoreactive protein (72 kD type IV collagenase) in primary skin melanoma. The Journal of Pathology. 1998; 186:51–58. [PubMed: 9875140]

18. Davidson B, et al. MMP-2 and TIMP-2 Expression Correlates with Poor Prognosis in Cervical Carcinoma--A Clinicopathologic Study Using Immunohistochemistry and mRNA in Situ Hybridization. Gynecologic Oncology. 1999; 73:372–382. [PubMed: 10366463]

19. Määttä M, Soini Y, Liakka A, Autio-Harmainen H. Differential Expression of Matrix Metalloproteinase (MMP)-2, MMP-9, and Membrane Type 1-MMP in Hepatocellular and Pancreatic Adenocarcinoma: Implications for Tumor Progression and Clinical Prognosis. Clinical Cancer Research. 2000; 6:2726–2734. [PubMed: 10914717]

20. Dubertret B, Calame M, Libchaber AJ. Single-mismatch detection using gold-quenched fluorescent oligonucleotides. Nat Biotech. 2001; 19:365–370.

21. Lee S, et al. A Near-Infrared-Fluorescence-Quenched Gold-Nanoparticle Imaging Probe for In Vivo Drug Screening and Protease Activity Determination. Angewandte Chemie. 2008; 47:2804–2807. [PubMed: 18306196]

22. Frank I, Tamm I. Coherent visible radiation of fast electraons passing through matter. Compt. Rend. Dokl. Akad. Mauk. SSSR. 1937; 14:109–114.

23. Xu Y, Piston DW, Johnson CH. A bioluminescence resonance energy transfer (BRET) system: application to interacting circadian clock proteins. Proc Natl Acad Sci U S A. 1999; 96:151–156. [PubMed: 9874787]

24. So MK, Xu C, Loening AM, Gambhir SS, Rao J. Self-illuminating quantum dot conjugates for in vivo imaging. Nat Biotechnol. 2006; 24:339–343. [PubMed: 16501578]

25. Quon A, Gambhir SS. FDG-PET and beyond: molecular breast cancer imaging. J Clin Oncol. 2005; 23:1664–1673. [PubMed: 15755974]

26. Beattie BJ, et al. Quantitative modeling of Cerenkov light production efficiency from medical radionuclides. PLoS One. 2012; 7:e31402. [PubMed: 22363636]

27. Kothapalli SR, Liu H, Liao JC, Cheng Z, Gambhir SS. Endoscopic imaging of Cerenkov luminescence. Biomed Opt Express. 2012; 3:1215–1225. [PubMed: 22741069]

28. Holland JP, Normand G, Ruggiero A, Lewis JS, Grimm J. Intraoperative imaging of positron emission tomographic radiotracers using cerenkov luminescence emissions. Mol Imaging. 2011; 10:177–186. [PubMed: 21496448]

Online Methods References

29. Holland JP, Sheh Y, Lewis JS. Standardized methods for the production of high specific-activity zirconium-89. Nucl Med Biol. 2009; 36:729–739. [PubMed: 19720285]

30. Holland JP, et al. Measuring the pharmacodynamic effects of a novel Hsp90 inhibitor on HER2/neu expression in mice using Zr-DFO-trastuzumab. PLoS One. 2010; 5:e8859. [PubMed: 20111600]

31. Cai W, Chen X. Preparation of peptide-conjugated quantum dots for tumor vasculature-targeted imaging. Nat. Protocols. 2008; 3:89–96. [PubMed: 18193025]

32. Institute of Laboratory Animal Resources (U.S.). NIH publication v. Bethesda, Md.: U.S. Dept. of Health and Human Services, Public Health Service; Committee on Care and Use of Laboratory Animals. Guide for the care and use of laboratory animals.

33. Flock ST, Jacques SL, Wilson BC, Star WM, van Gemert MJ. Optical properties of Intralipid: a phantom medium for light propagation studies. Lasers Surg Med. 1992; 12:510–519. [PubMed: 1406004]

34. Frank I, Tamm I. Coherent visible radiation of fast electraons passing through matter. Compt. Rend. Dokl. Akad. Mauk. SSSR. 1937; 14:109–114.

35. Rosenblum G, et al. Structural basis for potent slow binding inhibition of human matrix metalloproteinase-2 (MMP-2). J Biol Chem. 2003; 278:27009–27015. [PubMed: 12679334]
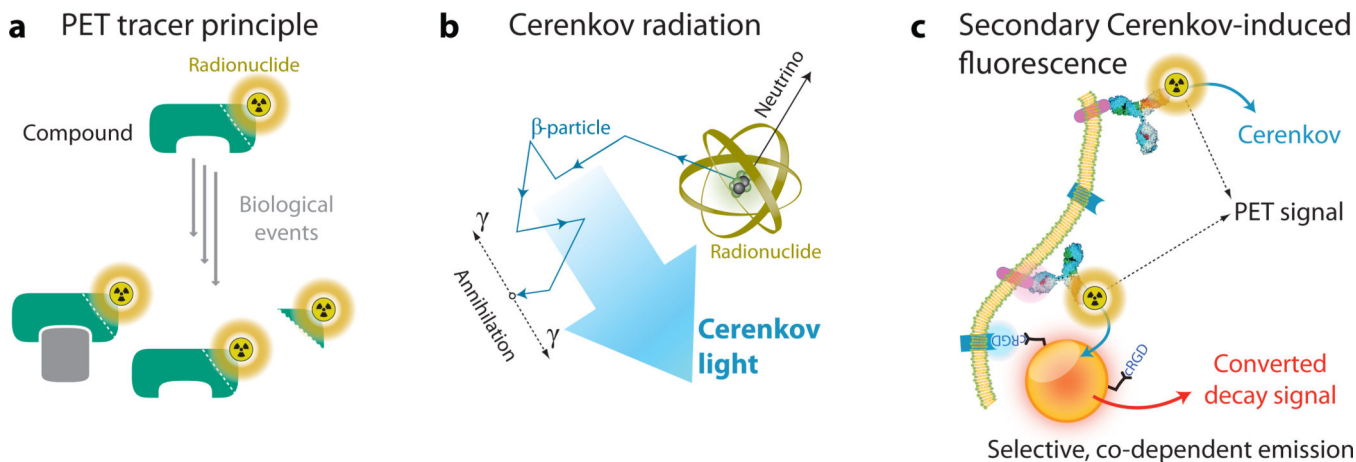
Figure 1. Conventional PET and Cerenkov Luminescence
PET tracer principle and the development of agents that fluorescently-convert the Cerenkov radiation optical decay signal. **(a)** Positron emission tomography (PET) enables high-sensitivity and quantitative imaging of whole-body tracer distribution. Unfortunately, radioactive probes are detectable regardless of their biological interactions; possibilities of which include binding, degradation or no change to the probe. This results in high background signal that is indistinguishable from accumulated probe. **(b)** Cerenkov luminescence (CL) is a result of charged particles moving through a dielectric medium faster than the speed of light in that medium. The high-energy particles polarize water molecules along their path. When these polarized molecules relax, they release a continuous wavelength luminescence centered in the blue. **(c)** This phenomenon can be harnessed to provide functional information regarding a radiotracer's *in vivo* fate. We can augment the depth of penetration of the blue-weighted light by using CR to excite fluorophores. Secondary Cerenkov-induced fluorescence imaging (SCIFI) can also be used in conjunction with activatable probes. This approach affords quantitative PET radiotracer information in addition to fluorescent reports of disease specific ligands and activities.
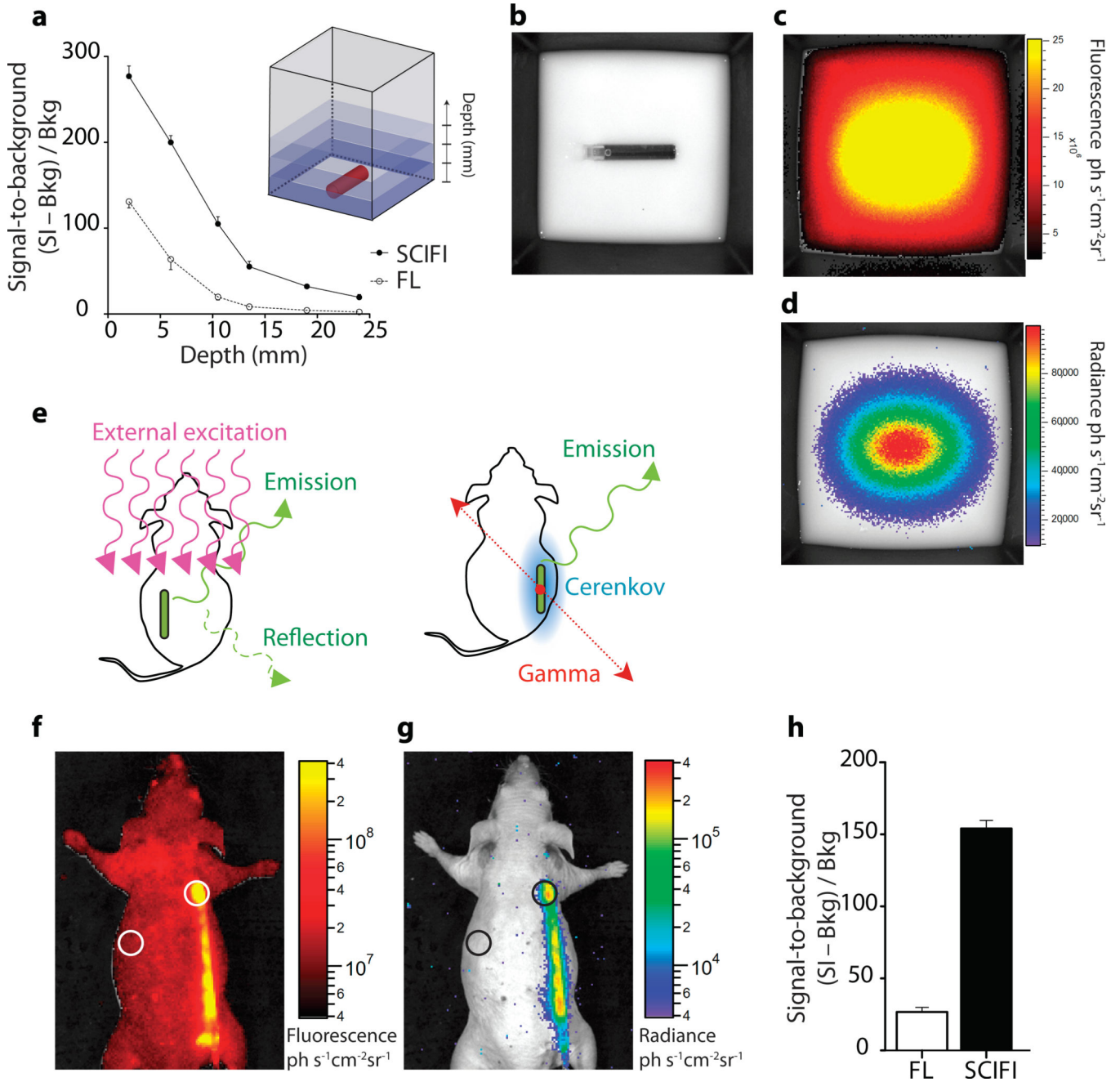
Figure 2. Fluorescence and Secondary Cerenkov-Induced Fluorescence
Comparison of the external excitation or CL-excitation of fluorophore. (**a**) Quantification of background subtracted signal-to-background (SB) measurements of an *in vitro* phantom of fluorescein and gallium-68 (140 μCi; 5.18 MBq) in a tissue scattering and absorbing mimic at increasing depth. Schematic shown at insert. (**b**) White light photograph of uncovered source in phantom. Representative figures of the filtered (500–520 nm) light emitted following (**c**) external laser, or (**d**) secondary Cerenkov-induced fluorescence. Note that the images display equal dynamic ranges. (**e**) The same principle applies using an *in vivo* subcutaneous capillary tube implantation model. The removal of the reflected and

background nonspecific excitation of endogenous fluorophores significantly reduces background. Representative acquisition of **(f)** externally laser-excited fluorophore and **(g)** [^{18}F]-FDG excited fluorescein. **(h)** The mean SB values of SCIFI (154.1±7) are approximately six–fold greater than that of conventional fluorescence (26.7±3.2).
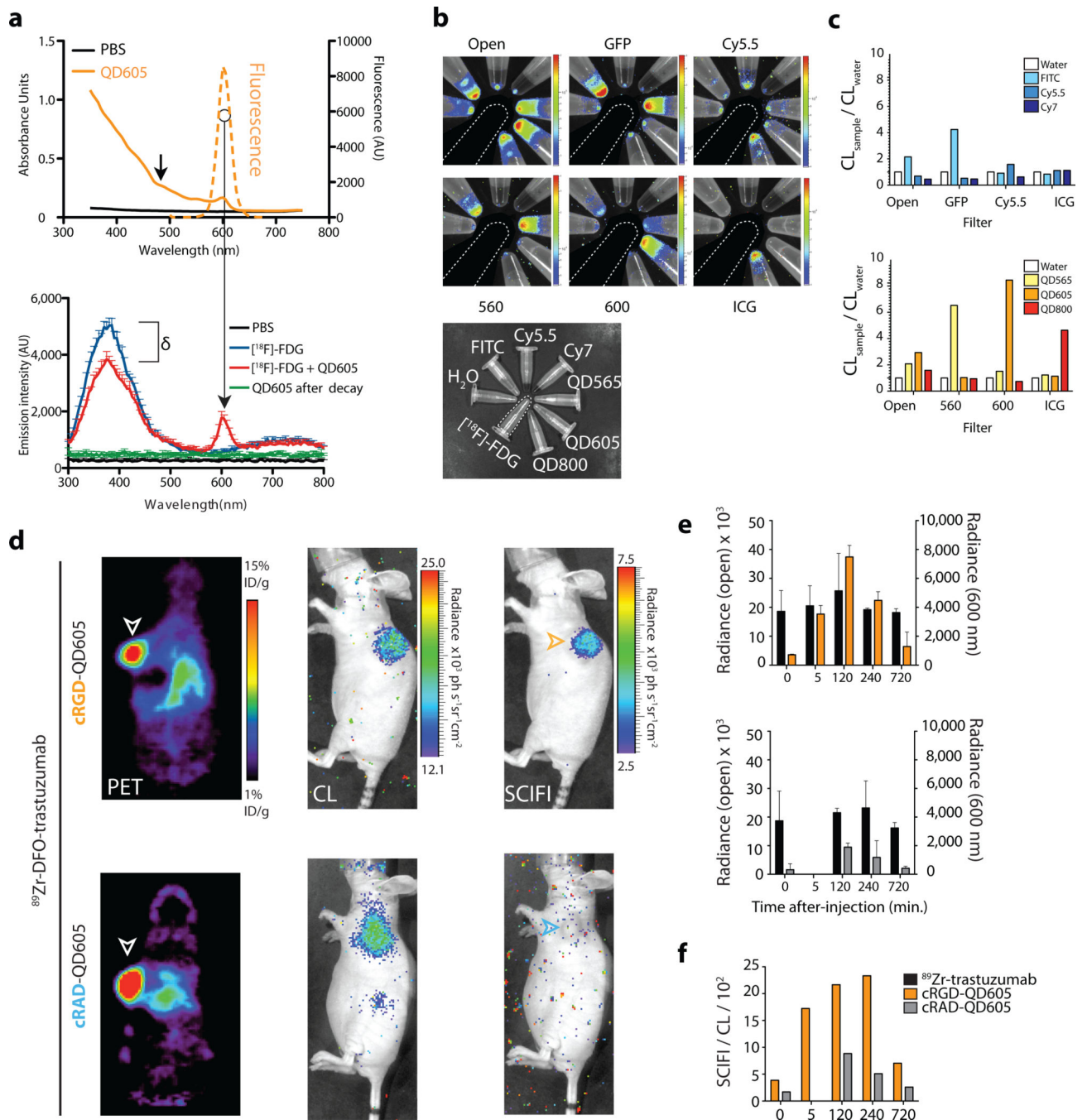
Figure 3. Secondary Cerenkov-Induced Fluorescence of Optical Probes
Multispectral and tandem Cerenkov-induced fluorescence emission for disease biomarker readout. **(a)** The absorbance and fluorescence profiles of QD605 (emission at 605 nm) are shown (upper panel) and the activation of the QD605 by [^{18}F]-FDG (27.75 MBq) through SCIFI (lower panel). The absorbance of some of the Cerenkov radiation is indicated by the difference between luminescence spectra prior to and after addition of QD (δ). **(b)** Filtered SCIFI for a panel of optical probes, FITC, Cy5.5, Cy7, QD565, QD605 and QD800 excited with an [^{18}F]-FDG source (14.8 MBq), along with a white light image as legend. See also

Supplemental Figure 2. **(c)** Quantification of the emission intensity, relative to control (water). The ratio of Cerenkov-induced fluorescence to control was greatest for QD605, used for further targeted SCIFI studies. **(d)** Coronal PET images show significant uptake of [^{89}Zr]-DFO-trastuzumab in Her2/neu expressing xenografts. This is also visualized with CL of the animals using no filter (open channel); sagittal orientation. In the 600 nm bandpass channel, the localization of the cRGD-QD605 targeting $\alpha_v\beta_3$ in the tumor microenvironment can be visualized as co-localized QD is excited by the CL from the radiolabeled antibody. The control cRAD-QD605 does not target to the tumor, and therefore shows no SCIFI signal. **(e)** CL and SCIFI quantification time-course. The CL signal is consistent across the imaging time-points, however the 600 nm signal increases in the cRGD-QD605 group, reaching a maximum at 120 minutes. **(f)** Ratiometric comparison of SCIFI signal to CL for the targeted and control groups over the time-course.
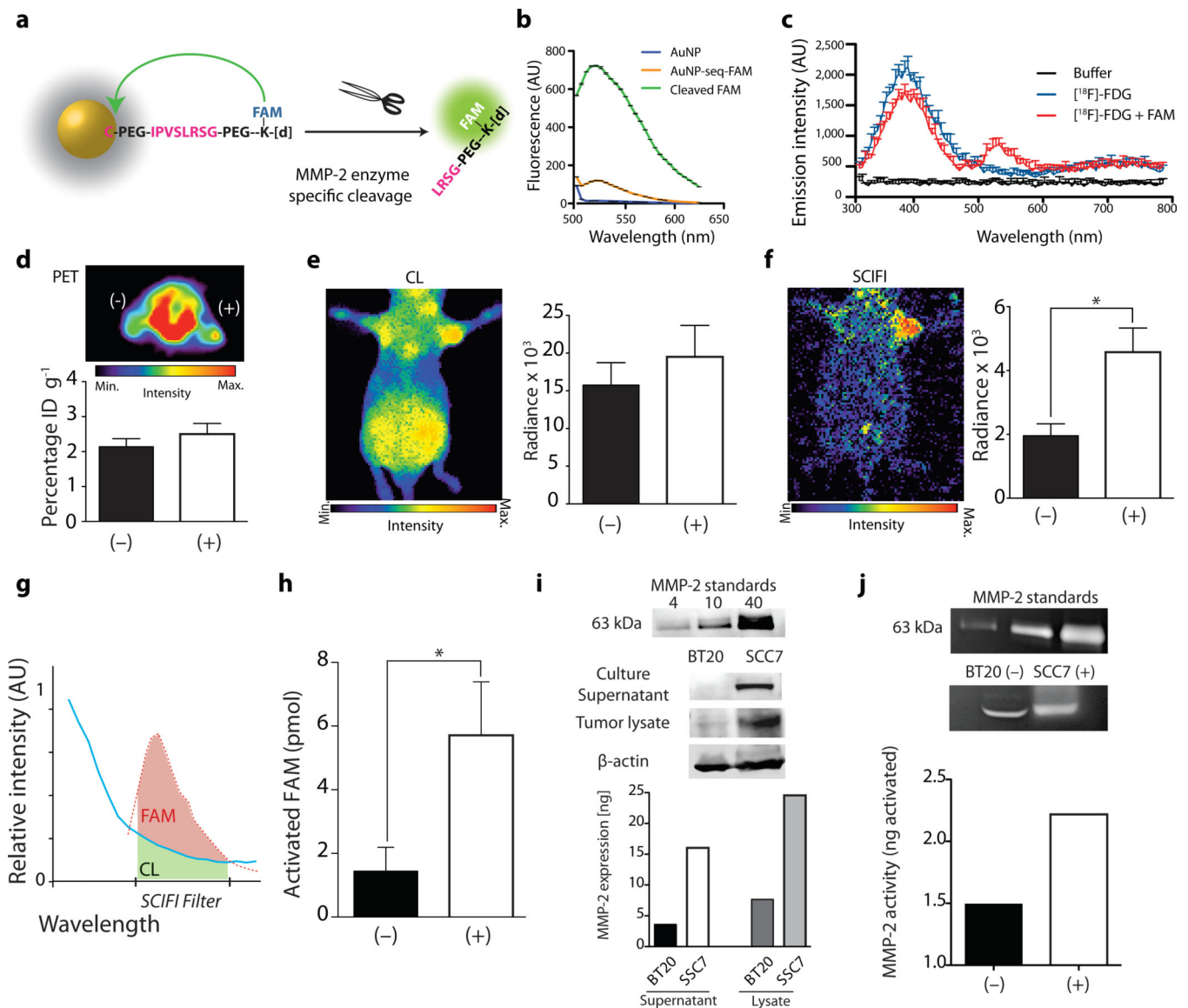
Figure 4. Enzyme Activatable SCIFI

Detection and quantitation of MMP-2 enzyme action using activatable secondary Cerenkov-induced fluorescence nanoparticles. **(a)** Schematic of enzyme activatable SCIFI probe. Fluorescence is quenched when the fluorescein (FAM)-bearing peptide is bound to the surface of the gold nanoparticle (AuNP). Enzymatic cleavage of the peptide by MMP-2 dissociates FAM, which is no longer quenched. **(b)** Fluorescent measurement of probe activation *in vitro* demonstrates recovery of signal after cleavage of the FAM from AuNP. **(c)** Spectra of activation of FAM probe using [18F]-FDG by SCIFI. **(d)** Axial PET imaging of [18F]-FDG uptake in both tumors showing non-statistically significant difference in uptake. **(e)** CL imaging of the Cerenkov signal recapitulates the PET readout of [18F]-FDG uptake. **(f)** The activated probe is detected in the enzyme-expressing tumor through SCIFI using a filter for FAM, demonstrating concomitant determination of enzyme and glycolytic activity. **(g)** Schematic representation of the components of observed signal in the SCIFI

channel. Quantitation of the probe activation can be accomplished by this approach because there is no non-specific autofluorescence or reflection, see also Supplemental Figure 5. **(h)** The amount of activated probe in the control tumor is 1.56 pmol, while in the enzyme expressing tumor the average activity is 6.23 pmol *(p<0.001)*. **(i)** Quantitative western blot of the activated MMP-2 enzyme expression in cell culture supernatant and from tumor lysate. We observe greater production of the active enzyme in the supernatant (left scale) than *in vivo* (right) from these representative samples. **(j)** Assessing the gelatinolytic activity of the enzyme (to degrade a gelatin containing gel) was determined by zymography, recapitulating the SCIFI findings.